

Article

Hydrogenation of Carbon Monoxide in the Liquid Phase: Influence of the Synthetic Methods on Characteristics and Activity of Hydrogenation Catalysts

Kalim A. Sheikh ^{1,2,*}, Ricki Drexler ¹, Thomas A. Zevaco ¹ , Jörg Sauer ¹  and Michael Bender ²

¹ Karlsruher Institut für Technologie (KIT), Hermann-von-Helmholtz-Platz 1, 76344 Eggenstein-Leopoldshafen, Germany

² BASF SE, Carl-Bosch-Straße 38, 67056 Ludwigshafen am Rhein, Germany

* Correspondence: kalim.sheikh@kit.edu

Abstract: Oxygenate fuels are a promising solution to urban air pollution, reducing soot emissions by big margins. Formaldehyde is a major building block for the synthesis of oxygen-rich fuels. Herein we report the synthesis, characterisation and testing of ruthenium on alumina catalysts for the methanol-mediated CO hydrogenation towards oxygenates with the formaldehyde oxidation state. We varied the synthesis parameters and could see interesting correlation between synthesis parameters, final metal loading, crystallite sizes and catalyst activity. The catalysts were tested in a high-pressure three-folded reactor plant in the CO hydrogenation in methanolic media. Interesting relationships between catalyst synthesis, structure and activity could be gained from these experiments.

Keywords: heterogeneous catalysts; hydrogenation catalysts; liquid phase; synthetic gas; ruthenium; nickel; temperature-programmed characterisation; CO hydrogenation; oxygenates



Citation: Sheikh, K.A.; Drexler, R.; Zevaco, T.A.; Sauer, J.; Bender, M. Hydrogenation of Carbon Monoxide in the Liquid Phase: Influence of the Synthetic Methods on Characteristics and Activity of Hydrogenation Catalysts. *Catalysts* **2023**, *13*, 482. <https://doi.org/10.3390/catal13030482>

Academic Editors: Shihui Zou and Juanjuan Liu

Received: 6 February 2023

Revised: 21 February 2023

Accepted: 22 February 2023

Published: 27 February 2023



Copyright: © 2023 by the authors. Licensee MDPI, Basel, Switzerland. This article is an open access article distributed under the terms and conditions of the Creative Commons Attribution (CC BY) license (<https://creativecommons.org/licenses/by/4.0/>).

1. Introduction

The transport sector is in the increasing focus of media and politics regarding its long-term sustainability. The greenhouse gas emissions in this sector stagnate in industrial countries, so the overall trend remains worrisome. Planning an extended electrification can be achieved only via additional infrastructures and a significant expansion of the power grid. An interesting interim solution might be the use of sustainable tailored synthetic fuels. Generated from synthesis gas and using either Fischer–Tropsch synthetic pathway, a methanol-based chemistry (methanol to X) or an upgrading of different biomass sources, both synthetic and conventional fuels inherit one major problem: the liberation of concerning fine particles, which are becoming a major problem in densely populated areas. Interestingly, fine soot particles and NO_x emissions are local emanations that can be markedly reduced by using oxymethylenethers (OME), which can be blended in large volume with conventional diesel fuels. These modern fuels reduce soot emission by more than 99% and can be synthesised using green methanol [1,2]. The current synthesis is energy-consuming and makes this type of fuel unaffordable for wide use. There are many synthesis routes to higher OMEs but the most efficient ones are achieved by reacting OME-1 (DMM, dimethoxy methane) with dry formaldehyde, mainly because no water has to be separated from the products [2].

In this publication, we want to focus on the first step of the synthesis the reduction of CO with H₂ to the formaldehyde oxidation state, which is a thermodynamically limited reaction. Recent works, among others studies of the Tanksale group [3,4], show that using liquid, protic media for this reaction provides an elegant solution to the thermodynamic barrier, by shifting the equilibrium towards products of formaldehyde stabilised with methanol or water (hemiformal or methylenglycols) [3]. The heterogeneous catalytic systems used in these studies involve a bimetallic combination of non-noble with noble

metals supported on different standard supports. We decided to focus on ruthenium as the active metal species and γ -Al₂O₃ as the support, considering that ruthenium has been proven for a long time to be highly active in CO hydrogenation reactions [5,6]. Surprisingly, the information gathered from the literature concerning synthetic ways to supported Ru catalysts (e.g., with high metal loadings) was revealed to be incomplete. Likewise, the search for reliable analytics able to encompass the main products obtained from the reaction of CO, H₂ and methanol was unsatisfactory. Both aspects were an incentive to develop a systematic approach and better understand both catalyst synthesis and reactions at work during CO hydrogenation performed in methanol. The focus will be put on relationships between synthesis parameters, morphology of the final material as well as on activity and selectivity of the catalyst under working conditions. A low-temperature approach was chosen for the evaluation of the catalysts because of the favourable thermodynamics of the CO hydrogenation reaction to the formaldehyde oxidation state and also because at higher temperatures ruthenium is highly active in catalysing the Fischer–Tropsch reaction. In addition, high pressures are needed to drive the reaction to the formaldehyde oxidation state [3], also increasing the solubility of the gases in the liquid phase. Theoretical studies dealing with density functional theory (DFT) have proven that formaldehyde is a plausible intermediate species in the synthesis of methanol in the presence of different metals [7]. Interestingly this leads to the conclusion that choosing the adequate reaction parameters in solution would lead preferentially to the formation of a “stabilised” formaldehyde, a hemiacetal, preventing the further hydrogenation to methanol.

In order to optimise the catalytic activity, it is paramount to understand the interplay between synthesis of the catalysts, morphology of the obtained crystallites (among others crystallinity, particle sizes and forms) and activity and selectivity of the catalysts. We focused on two different ruthenium precursors, with and without chloride, as well as on three synthetic procedures to produce the intended supported catalyst: co-precipitation, impregnation and adsorption. The widespread precipitation method is usually used for high metal loadings [8] and while being well-optimised, was not of interest in the current study. The impregnation and adsorption procedures are both more suitable for the synthesis of catalysts with low metal loadings [8]. Taking into account that we were aiming at intermediate loadings, we chose the impregnation method because it keeps counterproductive strong interactions between support and active metal to a minimum [8]. The most commonly used precursor for the synthesis of ruthenium on alumina catalysts is RuCl₃. For the sake of comparison we also used RuNO(NO₃)₃ [9], a chloride-free precursor, to better assess the effect of chloride on the catalyst structure and activity [10]. This particular method is well documented in the production of among others hydrogenation catalysts and bifunctional catalysts, e.g., hydrogenation and solid acid catalysts [8]. Nonetheless, the synthesis of supported ruthenium on alumina catalysts has been described in detail rather sporadically [8] most probably due to a problematic loss of ruthenium in the final supported catalysts observed during the necessary calcination step under air. The formation of numerous ruthenium oxides during the calcination step, among others ruthenium (VIII) oxide, is a recurrent problem owing to rather low decomposition temperatures of some of these compounds, reducing the ruthenium loading on the final catalysts [11].

2. Results and Discussion

The synthesis of the ruthenium pre-catalysts was performed using RuCl₃·xH₂O and Ru(NO)(NO₃)₃ (see Table 1) in different starting concentrations in order to reach the final metal loadings of 1, 3 and 5 wt% on a γ -Al₂O₃ support. The solutions of the ruthenium precursor in water were impregnated on the support according to the synthesis described elsewhere [3]. The same procedure was conducted for the synthesis of Ru–Ni systems supported on γ -Al₂O₃. According to the literature, the initial supported precursors need a further preparation step to actually bind the active metal particles to the supporting matrix. The role of the calcination was thoroughly described in the literature [12]. We opted for a static calcination under air, followed by a dynamic reduction step run under forming gas

(7–10 vol% H₂ in N₂) atmosphere (for details, see experimental section). Altogether ten final catalysts were isolated, characterised and submitted to a catalytic screening. The Ru-Ni catalysts were synthesised in a way that the final Ru loading would be 1 to 10 ruthenium to nickel. The amount of precursor needed to obtain a loading of 1 wt% of ruthenium was calculated from the XRF results obtained for the Ru on Al₂O₃ catalysts. For both ruthenium precursors, two RuNi catalysts were synthesised by differing the procedure after impregnation: the first one was reduced after impregnation (ir.) and the second one was calcined and then reduced (icr.). Tanksale et al. reported remarkable CO conversions to formaldehyde in liquid phase with the use of Ru-Ni on an Al₂O₃ system [3].

Table 1. Listing of the synthesised catalysts and the varied synthesis parameters.

Experiment	Precursor		Precursor Concentration [mM]		Final Catalyst
	Ru	Ni	Ru	Ni	
Ru-NO-1	*	-	5	-	Ru/ γ -Al ₂ O ₃ 1 wt%
Ru-NO-3	*	-	15	-	Ru/ γ -Al ₂ O ₃ 3 wt%
Ru-NO-5	*	-	24	-	Ru/ γ -Al ₂ O ₃ 5 wt%
RuNi-NO-ir.	*	‡	20	90	RuNi/ γ -Al ₂ O ₃
RuNi-NO-icr.	*	‡	30	80	RuNi/ γ -Al ₂ O ₃
Ru-Cl-1	°	-	5	-	Ru/ γ -Al ₂ O ₃ 1 wt%
Ru-Cl-3	°	-	15	-	Ru/ γ -Al ₂ O ₃ 3 wt%
Ru-Cl-5	°	-	24	-	Ru/ γ -Al ₂ O ₃ 5 wt%
RuNi-Cl-ir.	°	‡	20	90	RuNi/ γ -Al ₂ O ₃ 4 wt%
RuNi-Cl-icr.	°	‡	20	80	RuNi/ γ -Al ₂ O ₃ 6 wt%

Precursor: * = Ru(NO)(NO₃)₃ solution in dilute nitric acid (≥ 20 – $<30\%$), ° = RuCl₃·xH₂O solution in H₂O (4.7 wt% solution), ‡ = Ni(NO₃)₂·6H₂O.

The ruthenium loading was thoroughly determined after every step of the catalyst preparation. Interestingly, the accurate determination of ruthenium in complex matrices is known to be challenging as already reported in the literature [13,14]. The inductively coupled plasma coupled with optical emission spectrometry (ICP-OES), standardly used for metal content determination, could not deliver, even after complex sample preparation, reproducible results [15,16]. In comparison, X-ray fluorescence spectroscopy (XRF) gave dependable results after an easy sample preparation, allowing us to observe some trends as summarised in the following section [17].

2.1. X-ray Fluorescence Measurements of All Synthesised Catalysts

2.1.1. Pure Ruthenium Systems

None of the final catalysts had the expected loading of ruthenium according to XRF analysis. The absolute loss of ruthenium was lowest for the highest loaded catalysts (see Table 2). The calcination step was important to decompose the precursor and reduce the anion loading (nitrate and chloride) on the catalyst. For lower loadings of 1 or 3 wt%, the catalysts synthesised by impregnation of Ru(NO)(NO₃)₃ showed a lower loss of ruthenium than the catalysts synthesised by impregnation of RuCl₃, though for the highest loaded catalysts the trend was reversed. Calcination stabilises the ruthenium crystallites on the surface, because during calcination the crystals tend to agglomerate. The agglomerated crystals are thermodynamically more stable, because the total surface energy is lowered [18,19]. The change of the precursor from RuCl₃ to the Ru(NO)(NO₃)₃ was in this work a practical method to obtain a chloride-free catalyst. Solutions of RuCl₃ in water have a low pH and therefore chloride is able to incorporate into the Al₂O₃ lattice. These aluminium chloride bonds were highly stable and were not completely decomposed at calcination temperatures used in this study. The utilisation of chemical reduction methods is a way to generate appropriate chloride-free ruthenium catalysts; this synthetic pathway used in specific cases on an industrial scale is, however, scarcely documented. The formation of well-soluble alkali chloride salts is then the driving force for these preparation methods [20].

Table 2. XRF data for all ruthenium on γ -Al₂O₃ catalysts after calcination and reduction. (a) Impregnated-calcined; (b) impregnated-calcined-reduced (reduction: dynamic flow @ 450 °C with 5% H₂ in N₂ over 12 h.).

Catalyst	Ru (ic) ^a	Cl (ic) ^a	Ru (icr) ^b	Cl (icr) ^b
Ru-NO-1	0.28	-	0.08	-
Ru-NO-3	1.05	-	0.52	-
Ru-NO-5	1.60	-	0.67	-
Ru-Cl-1	0.47	0.11	0.15	0.10
Ru-Cl-3	1.44	0.12	0.60	0.12
Ru-Cl-5	2.58	0.18	1.82	0.19

2.1.2. Ruthenium-Promoted Nickel Systems

XRF measurements of the ruthenium-nickel catalysts showed similar results (see Table 3). As described earlier, ruthenium and nickel precursor were weighed to reach final loadings of 1 wt% for ruthenium and 10 wt% of nickel. As seen for the ruthenium on alumina catalysts, the calcination step reduced the ruthenium loading. Nickel, being a reactive and non-noble metal, is readily oxidised to form bulk NiO and stable nickel aluminate, NiAl₂O₄, as known from the literature [21,22]. Most of the nickel was then present as spinel structure in the catalyst, whereas a small share was present after calcination as bulk NiO on the surface of alumina. This nickel was available for H₂ during reduction and was reduced to nickel particles on the surface of alumina. Nickel, bound in the spinel structure, did not react with H₂ at our preparative reduction temperatures, so it remained embedded in the lattice structure of the support. This change in the structure of Al₂O₃ enhances the activity towards CO methanation or Fischer–Tropsch reactions [23,24]. The nickel loading is therefore stable all throughout the synthesis and increases only slightly from the calcined (NiO/NiAl₂O₄) to the reduced (Ni/NiAl₂O₄) state. The ruthenium loading for the RuNi-Cl catalyst was close to 1wt% but for the RuNi-NO catalyst the deviation of the nickel loading was bigger. One can conclude from this observation that the co-impregnation of ruthenium nitrosyl nitrate with nickel nitrate has an impact on the final ruthenium loading of the catalyst whereas the co-impregnation of ruthenium chloride with nickel nitrate has no impact on final ruthenium loading. For the ruthenium nitrosyl nitrate-impregnated catalysts, weak interactions between ruthenium and the support govern the outcome of the final ruthenium loading, whereas in the case of ruthenium chloride the final ruthenium loading is mainly governed by strong chloride bridges.

Table 3. XRF data for all RuNi on γ -Al₂O₃ catalysts after calcination (ic), and reduction (icr)/direct reduction (ir).

Catalyst	Calcined			Reduced		
	Ru	Ni	Cl	Ru	Ni	Cl
RuNi-NO-ir.	-	-	-	0.79	10.92	-
RuNi-NO-icr.	2.13	10.90	-	1.96	11.14	-
RuNi-Cl-ir.	-	-	-	1.42	11.16	1.06
RuNi-Cl-icr.	1.19	10.34	0.516	1.14	10.78	0.49

2.2. Powder X-ray Diffraction (XRD) and Scanning Electron Microscopy (SEM)

2.2.1. Pure Ruthenium Systems

X-ray diffractograms were recorded for all catalysts synthesised in this study. The Ru-XX catalysts are shown with different loadings and different precursors used for impregnation (Figure 1). No clear difference could be observed besides intensity differences, which were caused by the difference in loading. The reflexes for the amorphous γ -Al₂O₃ support can be seen and are overlaid with the ruthenium reflexes for the crystallite phases 100, 002 and 101 [25,26]. The reflexes for the ruthenium crystallite phases marked with

4, 5 and 6 are more isolated from the broad γ -Al₂O₃ reflexes, but show low intensity. For the catalysts with the lowest loading (black line), they are barely visible.

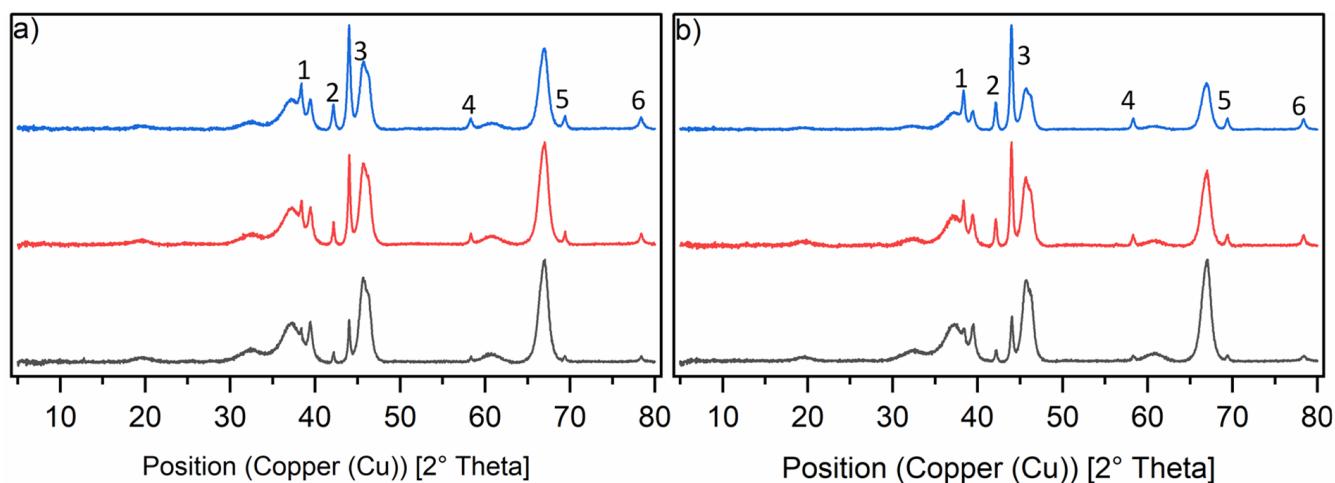


Figure 1. Normalised PXRD spectra of the six catalysts in the reduced state. Graph (a) shows the diffractograms of the Ru-NO-XX-icr. catalysts and Graph (b) shows the diffractograms of the Ru-Cl-XX-icr. catalysts. The black line shows the diffractograms of the Ru-XX-1 catalysts, the red line shows the diffractograms of the Ru-XX-3-icr. and the blue line shows the diffractograms of the Ru-XX-5-icr. catalysts. Ruthenium phases are marked in the diffractograms as follows: 1 = 100, 2 = 002, 3 = 101, 4 = 102, 5 = 110, 6 = 103.

Most of the reflexes were not suitable for the determination of crystallite size according to the Scherrer equation [27,28]. We chose the most intense reflexes and used them for the determination of peak width at half maximum (FWHM). From the FWHM value, the crystallite sizes for each phase were calculated and an average crystallite size could be thus estimated. The only trend observed from the data was that increasing the total loading of the catalyst led to a decrease in the average particle size to about 30 nm for both types of catalysts. Further increasing the ruthenium loading would cause an agglomeration of these particles to form bigger agglomerates (see Table 4).

Table 4. Crystallite size determination with Scherrer equation for the catalysts at the reduced state.

Catalyst	d (Ru ⁰) [nm] Average Crystallite Size
Ru-NO-1-icr.	54 ± 2
Ru-NO-3-icr.	33 ± 4
Ru-NO-5-icr.	30 ± 3
Ru-Cl-1-icr.	44 ± 3
Ru-Cl-3-icr.	37 ± 3
Ru-Cl-5-icr.	31 ± 1

Scanning electron microscopy (SEM) pictures (see Figure 2) of all ruthenium catalysts showed homogeneously distributed particles. For both type of catalysts, big agglomerates and clusters of ruthenium were visible (see Supplementary Material Figures S1–S8) but the overall dispersion for the Ru-NO-XX catalysts was higher. This is due to the presence of chloride bridges between the ruthenium atoms facilitating the agglomeration process [29]. Energy dispersive X-ray measurements showed that chloride was mostly present with the ruthenium particles.

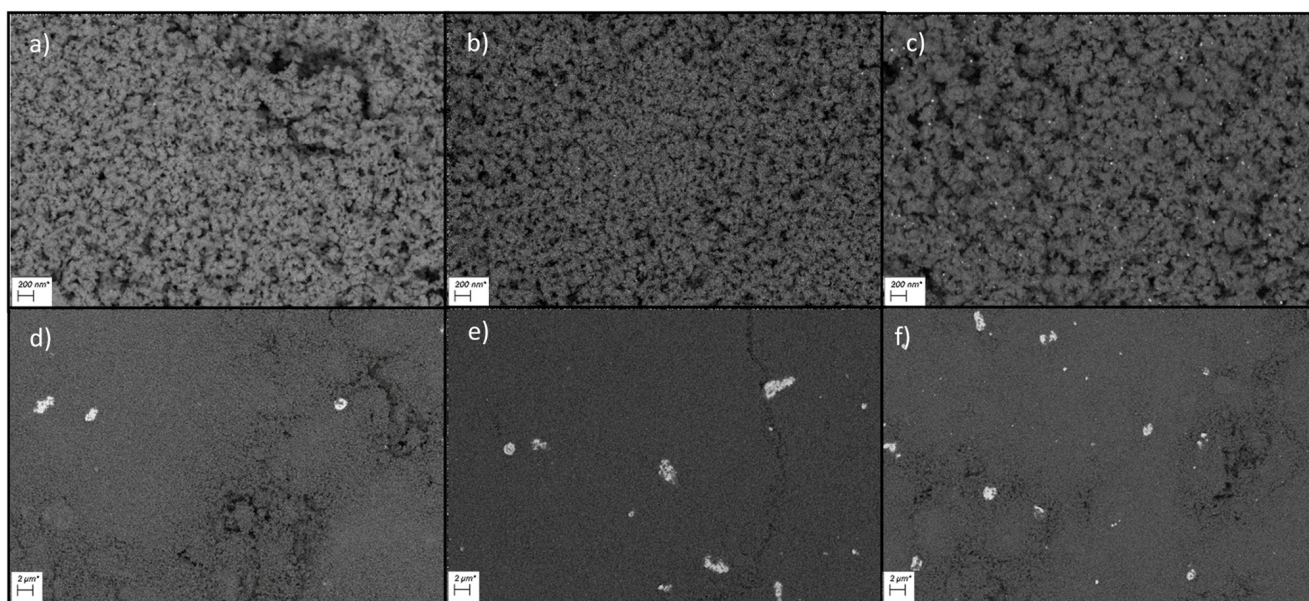


Figure 2. SEM Pictures of all six final Ru on Al_2O_3 catalysts. (a) = Ru-NO-1-icr., (b) = Ru-NO-3-icr., (c) = Ru-NO-5-icr., (d) = Ru-Cl-1-icr., (e) = Ru-Cl-3-icr., (f) = Ru-Cl-5-icr.

2.2.2. Ruthenium-Promoted Nickel Systems

The PXRD diffractograms (see Figure 3) for the RuNi-NO catalysts show interesting trends. The overall intensity for all ruthenium reflexes was much lower. The nickel reflexes show low intensity, because of the low amount of metallic nickel actually present on the surface of the catalyst. Most of the nickel was present as nickel aluminate spinel (NiAl_2O_4), which has similar reflexes to the $\gamma\text{-Al}_2\text{O}_3$ and can therefore not be distinguished from the support. The fact that the loading of the RuNi-NO-icr. catalyst was much higher than that of the Ru-NO-5-icr. catalyst, whereas the intensity of the ruthenium reflexes was lower, supports the statement that ruthenium was present in a bimetallic phase with nickel. For both RuNi-XX-icr. catalysts, metallic ruthenium reflexes can be seen like they appeared on the Ru-icr. catalysts. They show the same phases with same reflex positions. This suggests that besides a bimetallic phase of ruthenium and nickel, there was also metallic ruthenium present. Interestingly, the diffractogram of the RuNi-NO-ir. catalyst looks very different. Only a low-intensity reflex for the 111 nickel phase is apparent, whereas no NiAl_2O_4 could be found in this diffractogram. Regarding the RuNi-Cl-ir. catalyst, both ruthenium and metallic nickel phases are clearly observed. Most metallic nickel is apparent on the surface of the RuNi-Cl-ir. catalyst compared to all other RuNi catalysts. Besides the 111 nickel phase, which is overlaid with the ruthenium 101 phase, one can see broad reflexes of the 200 and 220 nickel phases, which only appear in very low intensity in the diffractogram of the RuNi-Cl-icr. catalyst.

Comparing the SEM-EDX pictures for the RuNi catalysts shows a very fine and homogenous distribution of the ruthenium and nickel particles for the RuNi-XX-ir. catalysts compared to the RuNi-XX-icr. catalysts. The addition of the calcination step during synthesis strongly favoured agglomeration processes leading to larger clusters of ruthenium. Nickel particles stayed homogeneously distributed even if calcined, but the amount of the nickel present at the surface as bulk NiO became smaller due to calcination. Furthermore, the energy dispersive X-ray spectroscopy clearly showed that chloride was present at the RuNi-Cl catalysts and was mostly bound to the ruthenium (see Supplementary Material Figures S1–S11).

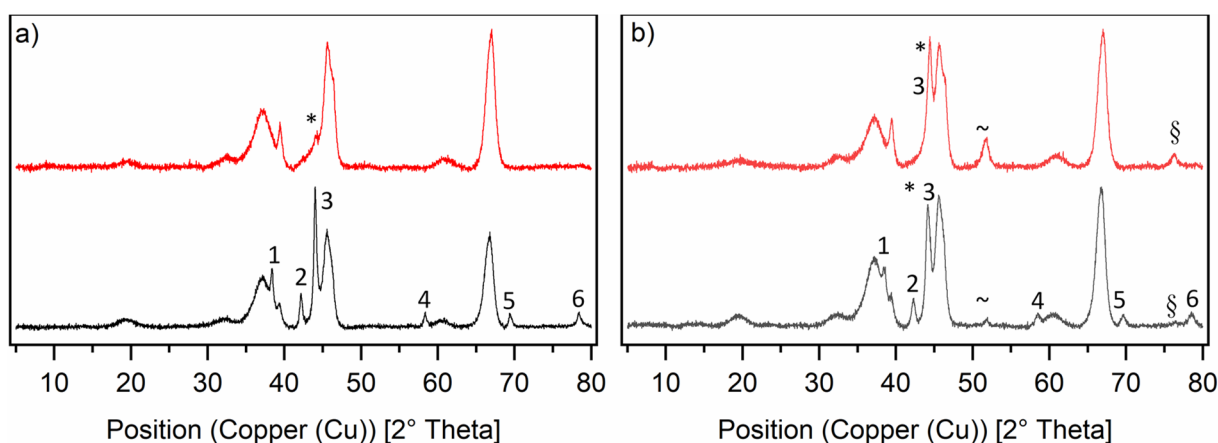


Figure 3. Normalised PXRD diffractograms of the ruthenium-nickel catalysts on γ - Al_2O_3 in reduced state. Graph (a) shows the RuNi-NO-catalysts and Graph (b) shows the RuNi-Cl-catalysts. The black lines show the RuNi-XX-ic. catalysts and the red lines show the RuNi-XX-ir. catalysts. The nickel phases are marked in the diffractograms as follows: * = 111, ~ = 200, § = 220. The ruthenium phases are marked in the diffractograms as follows: 1 = 100, 2 = 002, 3 = 101, 4 = 102, 5 = 110, 6 = 103.

2.3. Temperature-Programmed Reduction (TPR) and Temperature-Programmed Desorption (TPD) Studies

2.3.1. Pure Ruthenium Systems (TPR)

The temperature-programmed reduction (TPR) profiles were recorded for all calcined catalysts. Comparing the TPR profiles measured of the Ru-NO-ic. catalysts with the Ru-Cl-ic. catalysts shows a great impact of the used precursor and the loading on the reduction profile (see Figure 4). Unsupported RuO_2 shows a sharp reduction peak at $102\text{ }^\circ\text{C}$ [30]. Hosokawa et al. have reported that ruthenium(IV)-ions are reduced directly to ruthenium(0), thus the hydrogen consumption can be ascribed to the reduction of RuO_2 to Ru^0 [31]. The Ru-NO-ic. catalysts show two reduction signals, which suggests a bi-dispersive nature of the ruthenium oxide crystallites. The low-temperature reduction signal around $167 \pm 3\text{ }^\circ\text{C}$ corresponds to well-dispersed ruthenium(3+) with strong metal-support interactions being reduced to ruthenium(0) [21,32]. This ruthenium species is present at higher relative concentrations in materials with lower total loadings. This can be seen comparing the TPR-profiles of the Ru-NO-1-ic. catalyst to the higher-loaded catalysts, like Ru-NO-3-ic. or Ru-NO-5-ic. The high-temperature reduction signal at $197 \pm 3\text{ }^\circ\text{C}$ found for the Ru-NO-ic. catalysts corresponds to the reduction of bulk RuO_2 , these results matching well the results published by the group of Goldwasser et al. [12]. This high-temperature reduction peak corresponds to larger oxide particles. Goldwasser et al. observed the low-temperature reduction signal at $190 \pm 5\text{ }^\circ\text{C}$ and the high-temperature signal at around $223 \pm 4\text{ }^\circ\text{C}$. All these findings are also in good agreement with most publications [33,34]. Besides that, the TPR profile of the Ru-Cl-3-ic. catalyst shows a third, strong reduction signal between the LT- ($166\text{ }^\circ\text{C}$) and HT-Signals ($210\text{ }^\circ\text{C}$). This species also exists on the Ru-Cl-1-ic. catalyst but is just visible as a shoulder in the thermogram. The XRF data show that chloride was still present at the surface of the catalyst after calcination of the RuCl_3 -impregnated catalysts, the chloride ion bridging most likely two neighbouring Ru atoms. Some of these chloride bridges do not break at calcination temperatures under an air atmosphere. On the other hand, during reduction under TPR conditions (10 vol% H_2 in Ar) these bridges can be broken to form HCl and metallic ruthenium, as confirmed by the constant decrease of the chloride loading during reduction steps of all Ru-Cl-ic. catalysts. Literature studies could not resolve the reduction of these ruthenium chlorides at 181 to $187\text{ }^\circ\text{C}$ [12]. A mass-coupled thermogram would be interesting to show differences between HCl and H_2O generation during reduction of these chloride-loaded catalysts, but was not available during our studies.

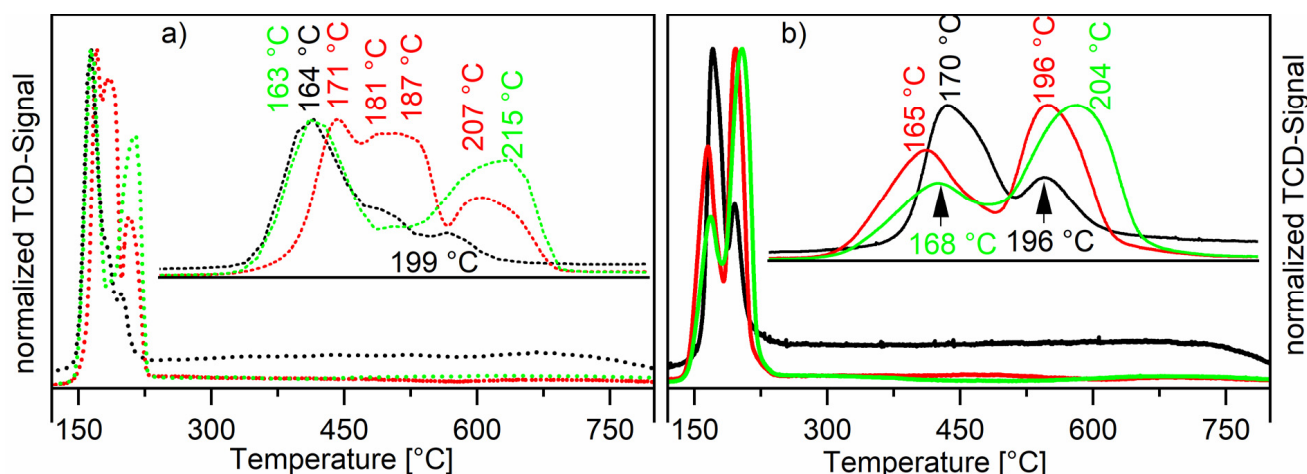


Figure 4. Normalised thermograms of the Ru-Cl-XX-ic. catalysts (Graph (a), dotted line) and Ru-NO-XX-ic. catalysts (Graph (b), compact line). The black line shows the thermograms of the Ru-XX-1-ic. catalysts, the red line shows the thermograms of the Ru-XX-3-ic. catalysts and the green line shows the thermograms of the Ru-XX-5-ic. catalysts.

2.3.2. Ruthenium-Promoted Nickel Systems (TPR)

The thermogram for the ruthenium-nickel system shows low-temperature reduction peaks for the reduction of ruthenium(IV) to ruthenium(0). The reduction of the nickel species varies also between RuNi-NO and RuNi-Cl catalysts (see Figure 5). The RuNi-NO thermogram is well explained in the literature [21]. The first two reduction peaks originate from the reduction of ruthenium as described earlier. The two broad reduction peaks at 448 and 768 °C arise from the reduction of nickel species. The broadness of the reduction peak at 448 °C can be explained by a major influence of ruthenium on the reduction of nickel and different interactions with the oxidic support. The formation of bimetallic compounds of nickel with reduction promoters like ruthenium can strongly decrease the reduction temperature of nickel oxides. This leads to a wide range of nickel particles starting with very fine particles, which are reduced easily and big particles with strong metal support interaction, which are reduced at higher temperatures. The uttermost case of this metal support interaction can be described by the reduction peak at 768 °C, which originates from the reduction of nickel(II) incorporated into the alumina structure as NiAl_2O_4 . This spinel structure is highly stable and shows a low availability for gaseous H_2 . Generally, the thermograms show that ruthenium and nickel reduce separately but also that a bimetallic species is present, easily reduced partly due to H_2 spillover effects, as suggested in the literature [35,36]. Interestingly, the RuNi-Cl catalysts do not show a similar broad 450 °C reduction peak. Three reduction peaks are observed instead, at lower temperatures (304, 352 and 391 °C). These signals originate from the interaction of ruthenium with nickel oxide, and therefore lower the reduction temperature for nickel oxide. Hydrogen is dissociatively adsorbed onto ruthenium very efficiently, forming a highly active reducing reagent. By migration of these hydrogen atoms to the neighbouring NiO species the overall barrier for the reduction of NiO is reduced and therefore the NiO reduction starts earlier [37,38]. It is, as this stage, not clear which role the remaining chlorides play in the lowering of the reduction and how the reduction of NiO regions in the bulk takes place. It seems, however, clear that this phenomenon is connected to a higher dispersion of NiO. Compared to the RuNi-NO catalysts, a higher share of nickel oxide seems to be stable NiAl_2O_4 , being thus part of the support and displaying a characteristic high-temperature reduction peak at 772 °C [39]. For details about the treatment procedure see catalyst characterisation part of Section 3.3.4.

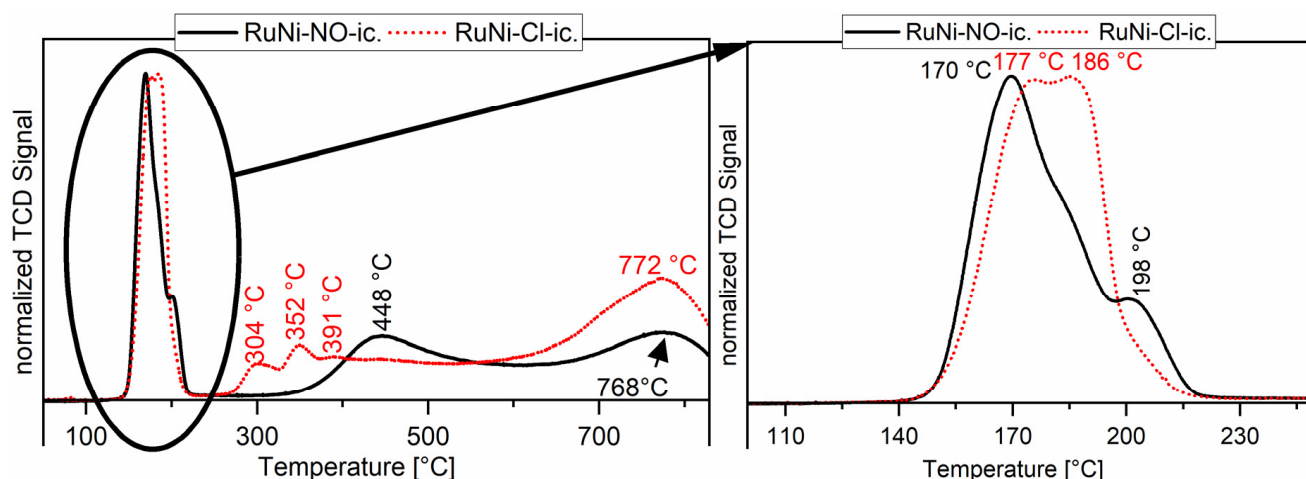


Figure 5. Temperature-programmed reduction of Ru/Ni on Al_2O_3 catalysts. The black line shows the thermogram recorded for the RuNi-NO-ic. catalyst and the dotted red line shows the thermogram recorded for the RuNi-Cl-ic. catalyst.

2.3.3. Comparison of H_2 Uptakes for Pure Ruthenium and Ruthenium-Nickel Systems (TPR)

Comparing hydrogen uptakes of all catalysts shows interesting results, as can be seen in Table 5. The fact that well-dispersed ruthenium was more present at low total Ru-loading can also be seen in the fact that the Ru-NO-1-ic. catalyst had high H_2 uptakes compared to the higher-loaded catalysts like Ru-NO-3-ic. The Ru-NO-3-ic. catalyst had 3.7 times the amount of ruthenium present but only had double the amount of H_2 uptake (see Table S1). This means that the total metal dispersion in the catalyst decreased from Ru-NO-1-ic. to Ru-NO-3-ic. For the higher-loaded chloride-containing catalysts, the H_2 uptake was generally higher, but in contrast to the nitrosyl-nitrate-impregnated catalysts, the metal dispersion of the Ru-Cl-1-ic. and the Ru-Cl-3-ic. catalysts stayed similar (total loading increased by a factor of 3 and the H_2 uptake also increased by a factor of 3). For both types of catalysts, however, NO or Cl, the dispersion decreased upon impregnation to reach the higher loadings (compare Ru-NO-1-ic. and Ru-NO-5-ic. or Ru-Cl-1-ic. and Ru-Cl-5-ic.). Regarding the mixed Ru/Ni catalysts, the low-temperature (LT) H_2 uptakes, which originate from the reduction of ruthenium, show comparable results to the ruthenium on alumina catalysts. Correlating with the loading of ruthenium, the pure low-temperature hydrogen uptake was lower than expected (theoretical loadings at similar dispersion to those of Ru/ Al_2O_3 catalysts: 1.334 for RuNi-NO-ic. and 1.309 for RuNi-Cl-ic.). This shows that not all of the ruthenium was present as bimetallic ruthenium-nickel species [21,36].

Table 5. H_2 uptake calculated from TPR profiles for the Ru- and Ru/Ni on Al_2O_3 catalysts.

Catalyst	H_2 Uptake [$\mu\text{mol/g}$]
Ru-NO-1-ic.	70
Ru-NO-3-ic.	150
Ru-NO-5-ic.	290
RuNi-NO-ic. (LT) *	230
RuNi-NO-ic. (HT) °	500
Ru-Cl-1-ic.	70
Ru-Cl-3-ic.	210
Ru-Cl-5-ic.	320
RuNi-Cl-ic. (LT) *	170
RuNi-Cl-ic. (HT) °	500

* = LT, low-temperature hydrogen uptake measured for the reduction peak for all ruthenium species, ° = HT, high-temperature hydrogen uptake measured for the reduction peak for all nickel species.

2.3.4. Temperature-Programmed CO Desorption–Pure Ruthenium Systems (CO-TPD)

Pulse titration with CO was measured with both ruthenium on alumina samples with intermediate loading (see Figure 6). Experimentally, the pulses could only be diluted down to 25% CO in He while keeping total flow in the system constant. This led to a fast saturation of the surface so the values calculated from these data were also low (see catalyst characterization part of Section 3.3.3).

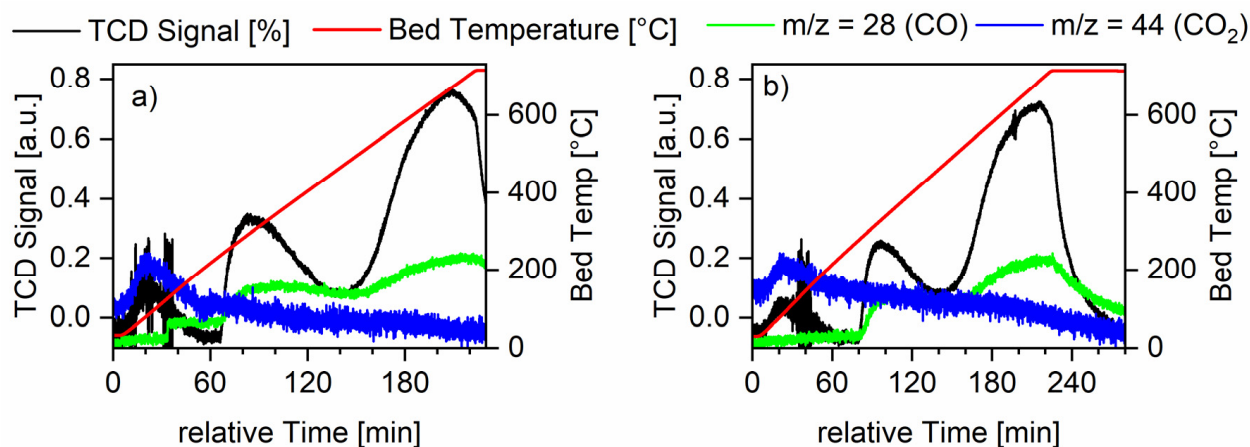


Figure 6. Temperature-programmed desorption of CO measurements for all Ru-XX-3 catalysts. The red line shows the temperature measured at the catalyst bed, the green line shows the mass spectrometer signal for the m/z value of CO, and the blue line shows the mass spectrometer signal for the m/z value for CO₂. Furthermore, the black line shows the TCD signal. Graph (a) shows the measurements for the Ru-NO-3-icr. catalyst and Graph (b) shows the measurements for the Ru-Cl-3-icr. catalyst.

For the sample Ru-Cl-3-icr., no decrease in pulse height could be observed from the first to the following pulses, meaning no CO adsorption could be measured and therefore no data could be obtained for dispersion, CO uptake or active surface area (ASA). From the CO desorption, maxima information about the structures and reactivity of the samples could be extracted (see Table 6). The TPD measurements showed a reactive surface area of ruthenium, which was actively adsorbing carbon monoxide. Two distinct desorption signals around 300 and 700 °C show a strong and a very strong adsorption of carbon monoxide onto the ruthenium surface. All in all, three desorption maxima could be observed. The first desorption maxima is linked to the only desorption of CO₂ and not CO. During this desorption, CO disproportionates to form CO₂ and C [40,41]. Because of the low dispersion on this catalyst, the carbon blocks the active sites very fast and therefore higher temperatures are needed to obtain a carbon-free active surface area. For the second desorption maxima, the Ru-NO catalyst shows a lower desorption temperature, meaning the CO was more loosely bound to this surfaces of ruthenium nanocrystals. CO tends to bind strongly on bridged adsorption sites. These are more present on catalysts with higher particles size, therefore confirming the trends observed with PXRD and SEM. The Ru-NO catalysts generally yielded smaller crystallite sizes.

Table 6. Data obtained from the temperature-programmed desorption of CO.

Catalyst	Monolayer CO Uptake [$\mu\text{mol/g}$]	Active Surface Area [m^2/g]	Desorption Maxima [$^{\circ}\text{C}$]	Dispersion [%]
Ru-NO-3-icr.	1.43	0.053	80/291/671	1.8
Ru-Cl-3-icr.	-	-	83/325/686	-

2.4. Catalyst Activity

As described earlier, the catalysts were screened related to their catalytic activity in CO hydrogenation performed in protic liquid media as described by Tanksale et al. [3].

The focus was put on the generation of formaldehyde. The chemistry of formaldehyde in solution is described by a complex system of equilibrium reactions. To simplify this reaction network, we used dry methanol as the solvent. This brings two major advantages. First of all, the hydrogenation of CO is prone to proceed over formaldehyde to methanol. Using methanol as the solvent, however, stops the further hydrogenation of the formaldehyde intermediate to methanol, because of the catalyst surface being “saturated” by methoxy species. Secondly, methanol acts as a stabilising agent for formaldehyde by generating quickly hemiformal species, which also stops further reactions of the highly reactive formaldehyde molecule. In a first approach, all catalysts were screened for their activity at 90 °C, 80 bar and using a 1:3 CO:H₂ gas mixture. The catalyst amount used in the test was varied according to their maximal theoretical loading. So catalysts with the theoretical loading of 1 wt% of ruthenium were added in the amount of 500 mg, the catalyst with the theoretical loading of 3 wt% of ruthenium were added in the amount of 167 mg and the catalysts with the theoretical loading of 5 wt% of ruthenium were added in the amount of 100 mg. After filling the reactors with catalysts and methanol under inert conditions, the gaseous compounds were dispensed via dedicated mass-flow controllers to the desired pressure. After heating the reactors to the desired temperatures, the reaction was started and liquid samples were regularly taken and analysed in an offline GC. This way of investigating the catalyst suspension in batch autoclaves, with various gas composition and temperatures, can be seen in this study as a standard test procedure to quickly evaluate the performance of a given system. However, regarding particularly the high cost of ruthenium, further investigation of the long-term stability and the potential recycling of the catalyst has to be taken into consideration [9].

A first exploratory test using all the Ru-XX catalysts gave an overview. An increase of the metal loading enhanced, as expected, the activity for both types of ruthenium catalysts, with small interesting nuances (see Figure 7). The Ru-Cl catalysts showed higher productivity than the Ru-NO catalysts. The highest productivity after 24 h was measured for the Ru-Cl-5-icr. catalyst with $45.2 \pm 0.4 \text{ mmol} \cdot \text{L}^{-1} \cdot \text{g}_{\text{cat}}^{-1}$. The determination of the ruthenium crystallites’ size confirmed these results. Increasing the metal loading led to a decrease in the crystallite sizes, an enhancement of the active surface and, concurrently, of the catalytic activity (see Supplementary Material Figure S1). No other products besides methylformate (MeFo) were detected at these temperatures. MeFo is generated under these experimental conditions by the insertion of carbon monoxide into methoxy groups present at the surface of the ruthenium crystallites. Hydrogen molecule cleavage does not play an active role at the surface of the catalyst at the used working temperatures. Higher synthesis gas conversions to C_x-compounds, for example, start at 200 °C [42].

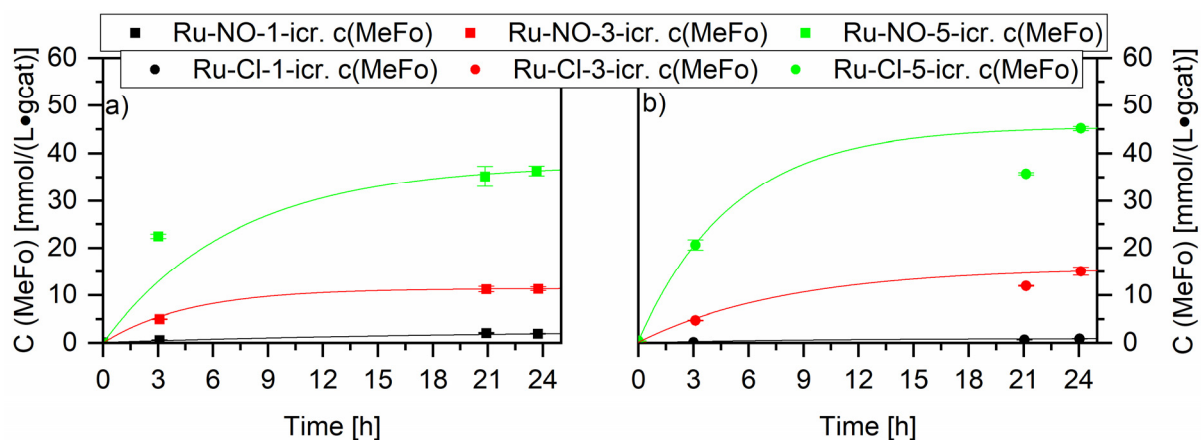


Figure 7. Screening experiments of different Ru loadings on Al₂O₃ tested in the methanol mediated CO hydrogenation reaction. Graph (a) compares the Ru on Al₂O₃ catalysts impregnated with Ru(NO)(NO₃)₃ (squares) and Graph (b) compares the Ru on Al₂O₃ catalysts impregnated with RuCl₃ (circles). Testing conditions: 80 bar, CO:H₂ 1:3, 90 °C, 50 mL methanol, quantification: GC-FID (PolyArc).

Similar screening experiments were carried out with the ruthenium-nickel catalysts (see Figure 8). A generally lower activity of the RuNi catalysts compared to the ruthenium catalysts was observed, indicating an inhibition effect of nickel, either due to the formation of an inactive alloy or to a lower intrinsic catalytic activity via stronger nickel-alumina support interactions. Interestingly, the RuNi-Cl-ir. catalyst with a very high chloride loading (1.06 wt%) led to the direct formation of dimethoxymethane (DMM) from synthesis gas and methanol. Tanksale et al. proposed that this reaction proceeds over the CO hydrogenation reaction towards formaldehyde, which in its reactive aldehyde form spontaneously reacts with the protic solvent, methanol, to form the hemiacetal [5,6]. The following acetalisation reaction, which is an acid-catalysed reaction forming water, is probably catalysed by the residual chloride traces. The results suggest that chloride loading on the alumina enhances its acidity and therefore is able to catalyse the further acetalisation reaction of the formaldehyde-hemiacetal (also known as hemiformal) to DMM and water [43]. We observed after 24 h a productivity towards DMM of $1.90 \pm 0.08 \text{ mmol} \cdot \text{L}^{-1} \cdot \text{g}_{\text{cat}}^{-1}$. Studies aiming for the synthesis of dimethoxymethane while using bifunctional catalysts observed productivities of $2.8 \text{ mmol} \cdot \text{L}^{-1} \cdot \text{g}_{\text{cat}}^{-1}$ after 20 h [6]. They used zeolite supports, more acidic than the alumina used in our study, strongly favouring the formation of dimethylether from the direct condensation reaction of methanol. Regarding methyl formate production, the established homogeneously catalysed synthesis is not directly comparable to this study [44].

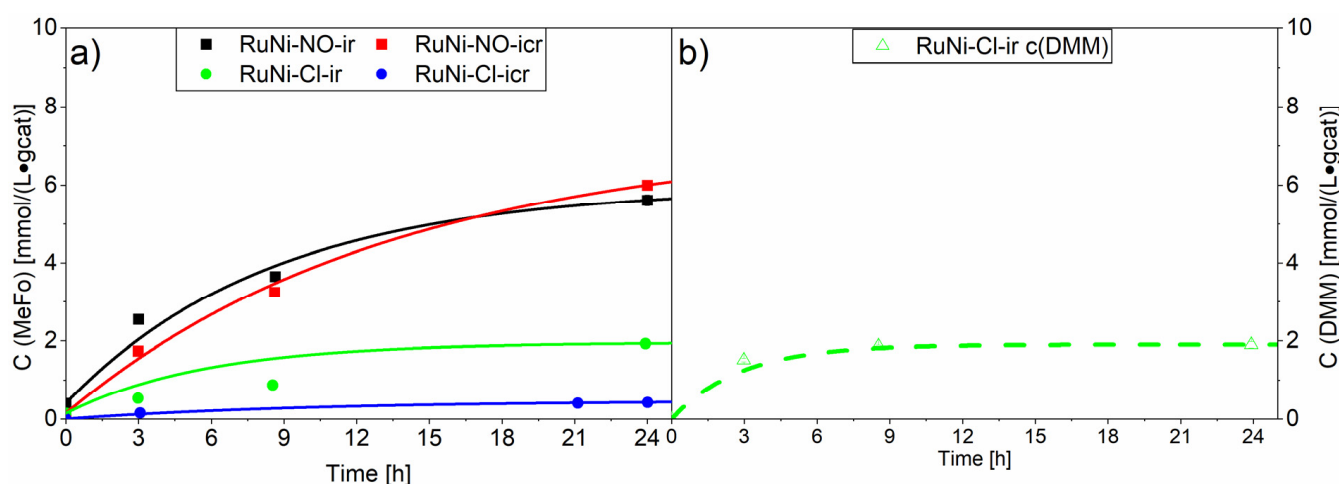


Figure 8. Results of screening experiments with the ruthenium-nickel on Al₂O₃ catalyst. The compact line shows the concentration for methylformate (a) and the dashed line shows the concentration of dimethoxymethane. (b) The concentrations generated with RuNi-NO catalysts are marked with squares whereas the concentrations generated with RuNi-Cl catalysts are marked with circles. Testing conditions: 80 bar, CO:H₂ 1:3, 90 °C, 50 mL methanol, quantification: GC-FID (PolyArc).

The variation of temperature led to an expected increase of the MeFo concentration to reach a plateau after ca. 24 h (see Figure 9). Two of the highest-loaded ruthenium catalysts were chosen. The Ru-NO-5-icr. catalyst displayed the highest productivity after 24 h with $950 \pm 10 \text{ mmol} \cdot \text{L}^{-1} \cdot \text{g}_{\text{cat}}^{-1}$, whereas for the Ru-Cl-5-icr. catalyst the productivity reached $885 \pm 17 \text{ mmol} \cdot \text{L}^{-1} \cdot \text{g}_{\text{cat}}^{-1}$. This trend in favour of the Ru-NO catalysts was observed for all temperatures beside 90 °C. For both catalysts, no major side reactions could be observed even at 150 °C.

Besides temperature variation, a vast variation of CO partial pressure was conducted with the Ru-NO-5-icr. catalyst, which led to the highest MeFo concentrations around $3.4 \pm 0.1 \text{ mmol} \cdot \text{L}^{-1} \cdot \text{g}_{\text{cat}}^{-1}$ after 24 h. This productivity was reached using a 90% CO and 10% H₂ gas mixture. As methyl formate is formed by the reaction of methanol and CO, H₂ can be seen as only diluting the reaction mixture and as playing no direct role in this reaction. By reducing its partial pressure, you would expect an increase of the MeFo productivity. A 100% CO run was carried out to confirm this, using argon to keep the

total pressure constant (CO:Ar 1:1). The good solubility of argon in methanol, better than hydrogen's, led indirectly to a higher amount of CO being dosed to reach the same pressure. That explains the higher productivity of the 50% Ar towards the 50% H₂ run. If the CO amount in solution would have been kept constant, the total productivity of the 1-to-1 Ar/H₂ run would be comparable (see Figure 10).

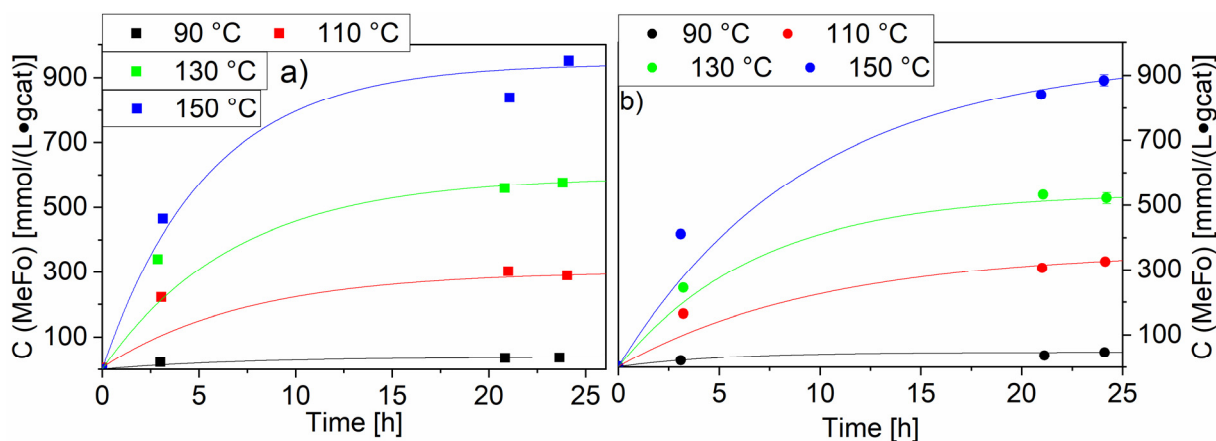


Figure 9. Impact of the temperature on the methyl formate productivity with Ru-NO-5-icr. and Ru-Cl-5-icr. used as catalysts. Graph (a) shows the MeFo concentration for the Ru-NO-5-icr. Catalysts, Graph (b) shows the methylformate concentration for the Ru-Cl-5-icr. catalyst. Testing conditions: 80 bar, CO:H₂ 1:3, 50 mL methanol, quantification: GC-FID (PolyArc).

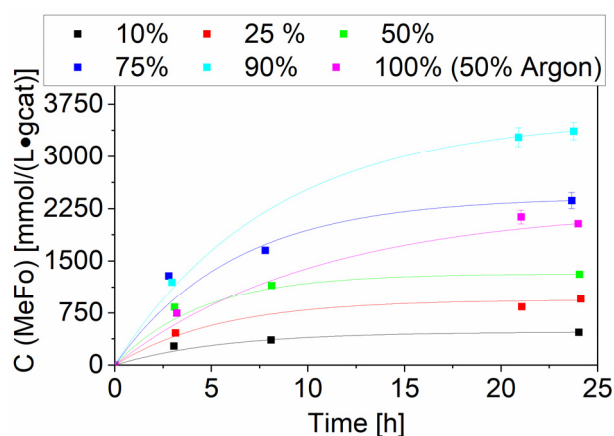


Figure 10. Variation of CO partial pressure for the Ru-NO-5-icr. catalyst. Testing conditions: 80 bar, 150 °C, 50 mL methanol, quantification: GC-FID (PolyArc).

A temperature variation was carried out with both RuNi-XX-ir. catalysts in order to understand the effect of nickel on the catalytic activity of the mixed ruthenium/nickel catalyst. As described earlier, both showed a lower activity than the Ru-XX catalysts, with the highest MeFo activity observed in these runs at 130 °C with the RuNi-NO-ir. catalyst with concentrations up to $29.7 \pm 0.6 \text{ mmol} \cdot \text{L}^{-1} \cdot \text{g}_{\text{cat}}^{-1}$ (see Figure 11).

The RuNi-Cl-ir. catalyst as observed at 90 °C catalysed the direct formation of DMM from methanol and synthesis gas. This exothermic reaction is in an equilibrium state after 24 h of operation [5,6]. Therefore, the increase of the temperature leads to a decrease in equilibrium concentration of DMM as observed in Figure 12. A continuous removal of water from the reaction mixture could increase the equilibrium concentration of DMM. This has been achieved by Tanksale et al. in a CO₂ hydrogenation reaction directly to DMM by using molecular sieves [5].

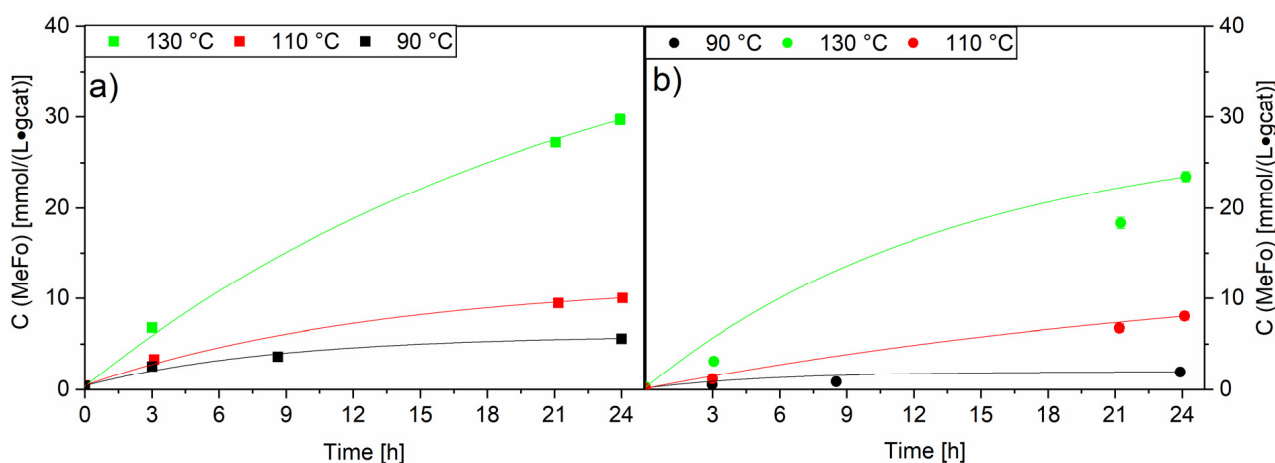


Figure 11. Comparison of temperature variation for RuNi-NO-ir. (Graph (a)) and RuNi-Cl-ir. (Graph (b)) catalysts. Solid lines (filled squares and circles) show concentration of methylformate. Black lines show the concentrations generated at 90 °C, red lines show the concentrations generated at 110 °C and green lines show the concentrations generated at 130 °C. Testing conditions: 80 bar, CO:H₂ 1:3, 50 mL methanol, quantification: GC-FID (PolyArc).

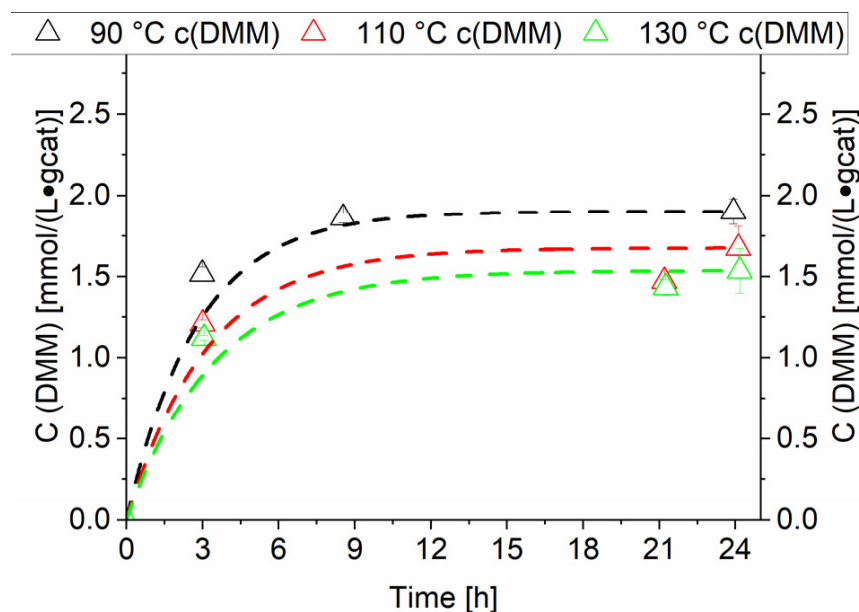


Figure 12. Comparison of temperature variation for RuNi-Cl-ir. catalyst. Dashed lines (unfilled triangles) show concentration of dimethoxymethane. Black lines show the concentrations generated at 90 °C, red lines show the concentrations generated at 110 °C and green lines show the concentrations generated at 130 °C. Testing conditions: 80 bar, CO:H₂ 1:3, 50 mL methanol, quantification: GC-FID (PolyArc).

3. Materials and Methods

3.1. Materials

Chemicals and materials were supplied by Alfa Aesar^A (Kandel, Germany), abcr GmbH^{abc} (Karlsruhe, Germany), Merck KGaA^M (Darmstadt, Germany), Air Liquide^{AL} (Düsseldorf, Germany) and Thermo Scientific^{TS} (Karlsruhe, Germany) and used without further purification. The values in brackets show the purity and other properties.

Ruthenium(III)chloride hydrate (99.9%)^{abc}, ruthenium-nitrosylnitrate solution in dilute nitric acid (4.7 wt%)^{TS}, nickel nitrate hexahydrate (98%)^A, gamma-aluminium oxide (99.97%, 80–120 m²/g)^A, carbon monoxide (99.97%, 200 bar, 40 l)^{AL}, hydrogen (99.999%, 300 bar, 50 l)^{AL}, argon (99.9999%, 200 bar, 50 l)^{AL}, methanol (99.8%, extra dry over molecu-

lar sieves)^{TS}, Dimethoxymethane ($\geq 99.50\%$)^{TS}, Methylformate ($\geq 97\%$)^{TS}, p-formaldehyde (≥ 95.0)^M.

3.2. Catalyst Synthesis

The catalysts were synthesised by wet impregnation of the metal precursor solution onto the γ -Al₂O₃ support by slightly adapting the literature procedure [3]. The variation between the RuCl₃ × H₂O precursor and the Ru(NO)(NO₃)₃ precursor and the variation of the final metal loading was conducted by keeping the amount of water and amount of γ -Al₂O₃ constant (70 mL in 4 g), therefore changing the concentration of the precursors to achieve a higher final loading. After wet impregnation (60 °C, 16 h) and drying (rotary evaporator, 50 mbar, 200 RPM, 50 °C → static oven, 120 °C, 16 h) the catalysts were calcined in a static oven at 600 °C (6 h, 10 K/min). The prior-described calcined powders were then reduced in a tube furnace at 450 °C (6 h, 7 K/min) in a forming gas atmosphere (7–10% H₂ in N₂, 4 sml/min), then kept at 450 °C for an additional hour under an argon stream and cooled down to room temperature. The obtained powders were stored under an argon atmosphere and used for characterisation and screening.

3.3. Catalyst Characterisation

The catalysts were characterised with different techniques. For the determination of the actual loading of the Ru metal on the support, X-ray fluorescence spectroscopy (XRF) was used. For the determination of the lattice structure and the crystallite size, we used powder X-ray diffraction spectroscopy and scanning electron microscopy (SEM) coupled with an energy dispersive X-ray detector (EDX). For the chemisorption studies, we chose temperature-programmed desorption with CO and temperature-programmed reduction with H₂ to further analyse active surface area and reductive species.

3.3.1. X-ray Fluorescence Spectroscopy (XRF)

In contrast to ICP-OES, XRF can directly analyse a wide range of elements without time-consuming preparation techniques. The calcined samples (200–500 mg) were analysed for their Al, Ni and Ru content. The samples were measured in a Bruker S4 Pioneer spectrometer (Bruker, Karlsruhe, Germany) preliminarily prepared as powders on a Mylar foil and using a dedicated 34 mm collimator mask for the measurements.

3.3.2. Powder X-ray Diffraction (PXRD)

PXRD was carried out with a PANalytical X'Pert Pro X-ray diffractometer (Bragg-Brentano geometry with Cu K α radiation and a Ni filter/Malvern Panalytical, Malvern, UK). The range between 5 and 80° was measured within 2 h. The diffraction patterns were compared to reference compounds from the Joint Committee of Powder Diffraction Standards (JCPDS) database. The samples were measured both in calcined and reduced state. Minimal exposure to air during the measurements of the reduced catalysts could not be avoided due to the used setup, but the trends for the crystallite size determination are still meaningful. Reflections of the calcined and reduced catalysts were assigned to the following JCPDS references [25,45–47]. The K-Alpha 1 line and a K-Factor of 0.90004 were used for calculations. The reflexes were fitted with X'Pert HighScore and the line broadening of the instrument was calculated from a calibration sample containing lanthanum hexaboride.

3.3.3. Temperature-Programmed Desorption of CO (CO-TPD)

TPD measurements were taken with 3P Instruments (3P Instruments GmbH & Co. KG, Odelzhausen, Germany). At the AMI-300 Serie a pulse titration with CO was measured. The samples were taken from the reduced state and treated as described in Table 7.

Table 7. Treatment Procedures for the CO-TPD measurements.

Treatment	Procedure	Remark
1	Gas: 5% H ₂ /Ar Flow: 50 mL/min Ramp: 30 °C → 450 °C Rate: 10 K/min Hold 300 min	Reduction
2	Gas: Ar Flow: 50 mL/min Temp.: 450 °C Hold: 60 min Cool down to 30 °C Hold 10 min	Purging after reduction
3	Gas: 25% CO/He Puls (15 times) Gas: He Flow: 10 mL/min Temp.: 30 °C	Pulse titration
4	Gas: He Flow: 50 mL/min Temp.: 30 °C Hold: 15 min	Purging after saturation
5	Gas: He Flow: 30 mL/min Ramp: 3 K/min Hold: 60 min	Temperature-programmed desorption (TPD)

3.3.4. Temperature-Programmed Reduction (TPR)

TPR measurements were carried out at the AMI-300 Serie (3P Instruments GmbH & Co. KG, Odelzhausen, Germany). The samples were taken from the calcined state and treated as described in Table 8.

Table 8. Treatment procedures for the TPR measurements.

Treatment	Procedure	Remark
1	Gas: Ar Flow: 30 mL/min Ramp: 30 °C → 200 °C Rate: 10 K/min Hold 15 min	Drying at 200 °C/purging
2	Gas: Ar Flow: 30 mL/min Ramp: 200 °C → 30 °C Rate: 10 K/min Hold 20 min	Back to 30 °C/purging
3	Gas: 10% H ₂ /Ar Flow: 30 mL/min Temp.:30 °C; Hold 5 min Ramp: 30 °C → 850 °C Rate: 5 K/min Hold 10 min	Temperature-programmed reduction (TPR)

3.4. Catalyst Activity Tests

Further comparison of the catalysts was performed with a high-pressure parallel screening apparatus. The so-called “PASCAR” (for PARallel Screening of Catalytic Reactions) plant is a 3-folded batch reactor plant which can be used to evaluate catalytic

reactions and monitor the formation of specific compounds via offline analytics, the reactions taking place ideally in liquid phase. This plant was optimised together with the GC analytics (*vide infra*) to reach a high reproducibility of the results gathered during the study of methanol-mediated CO hydrogenation reactions. The three reactors originally from the Parr Instrument Company have separate gas (H_2 , CO and Ar) and liquid dosing systems. The three reactors can be individually purged with argon to remove residual air/moisture potentially present in the system. The testing gear is designed to use several solvents as gradient; however, only methanol was used for this study. The solvent and reactant were dosed gravimetrically with a HPLC Pump. H_2 , CO and Ar can be exactly dispensed with a mass-flow controller (Bronkhorst, Wagner MSR GmbH, Offenbach, Germany) and mixed in specific amounts. After inert transfer of the *ex situ*-reduced catalyst into the reactor, a self-written HiText (LabVision 2.15.1.17, proprietary process control system from HiTec Zang GmbH, Herzogenrath, Germany) recipe was started. It automatically delivers the needed amount of methanol into each reactor followed by the required amount of gases, and pressurises the reactors (if needed) with argon to reach the desired starting pressure. Each reactor is then heated with a specific mantle to the predetermined temperature (up to 200 °C). The temperature of the reaction mixture is recorded via a specific thermocouple, independent from the thermocouple responsible for the heating mantle. A flow chart showing all the necessary components of the PASCAR plant can be found in Figure 13. The catalyst activity tests were conducted based on the literature, but the procedure was adjusted to the PASCAR plant [48]. Due to a high degree of automation, the adaptation of the process was fed into the system by changing the recipe. We have studied sequential dosing of liquid and gaseous compounds as well as parallel dosing and found that the procedure described above is ideal for these types of reactions.

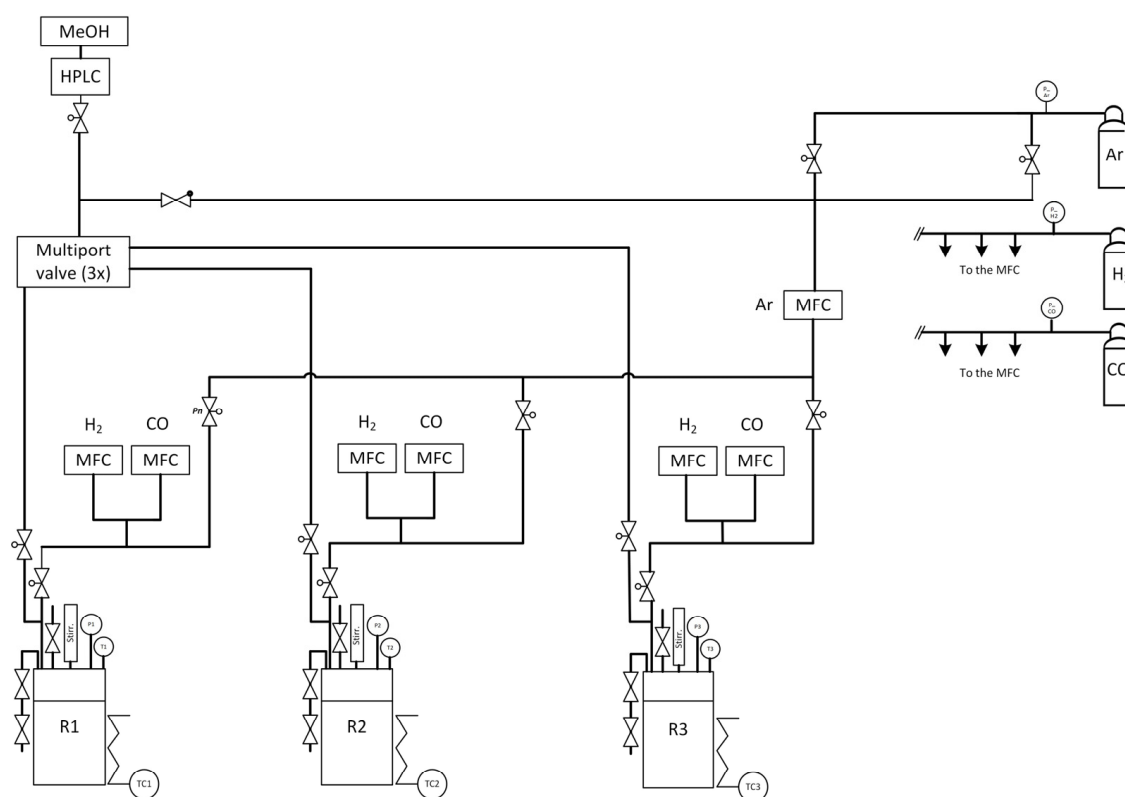


Figure 13. Flow chart of the PASCAR plant with all important devices.

3.5. Process Analytics

For the analysis of the products, a specific offline-GC FID (Agilent Technologies GC 8890, Waldbronn, Germany) with an autosampler (50 Position Autoinjector, Agilent

Technologies G4567A, Agilent Technologies, Waldbronn, Germany) was used. The use of a dedicated Dean's switch device is mandatory in order to protect the detector from a methanol overload (as we were systematically working with methanolic solutions). The injection temperature was kept at 180 °C, with a split ratio of 50:1. The starting temperature for the oven was 40 °C, which was held for 2 min and then heated at 25 K/min to 180 °C, the columns used were a combination of DB-Wax Ultra inert (30 m, 0.32 mm, 0.5 µm, Agilent Technologies, Waldbronn, Germany) and a deactivated column after the Dean's switch. A total run time of 7.6 min allowed a fast analysis of liquid samples and gave good separation for methanol, dimethoxymethan, methylformate and formaldehyde (p-Formaldehyde dissolved in boiling dry methanol). Fischer-Tropsch products were not observed under these mild conditions. To overcome the problem of a low intrinsic response factor of the expected components in the FID, a PolyArc methaniser reactor was intercalated between column and FID. This micro-reactor has two chambers, one for the oxidation of carbon-containing analytes to CO₂ and a second for the complete methanisation of CO₂. This gives the advantage of having the same response factor for all carbon-containing compounds present in the mixture. The Dean switch can be configured to vent out the solvent signal to increase the lifetime of the catalysts used in the PolyArc and to prevent overloading. A flow path diagram of the optimised GC can be seen in Figure 14 [49].

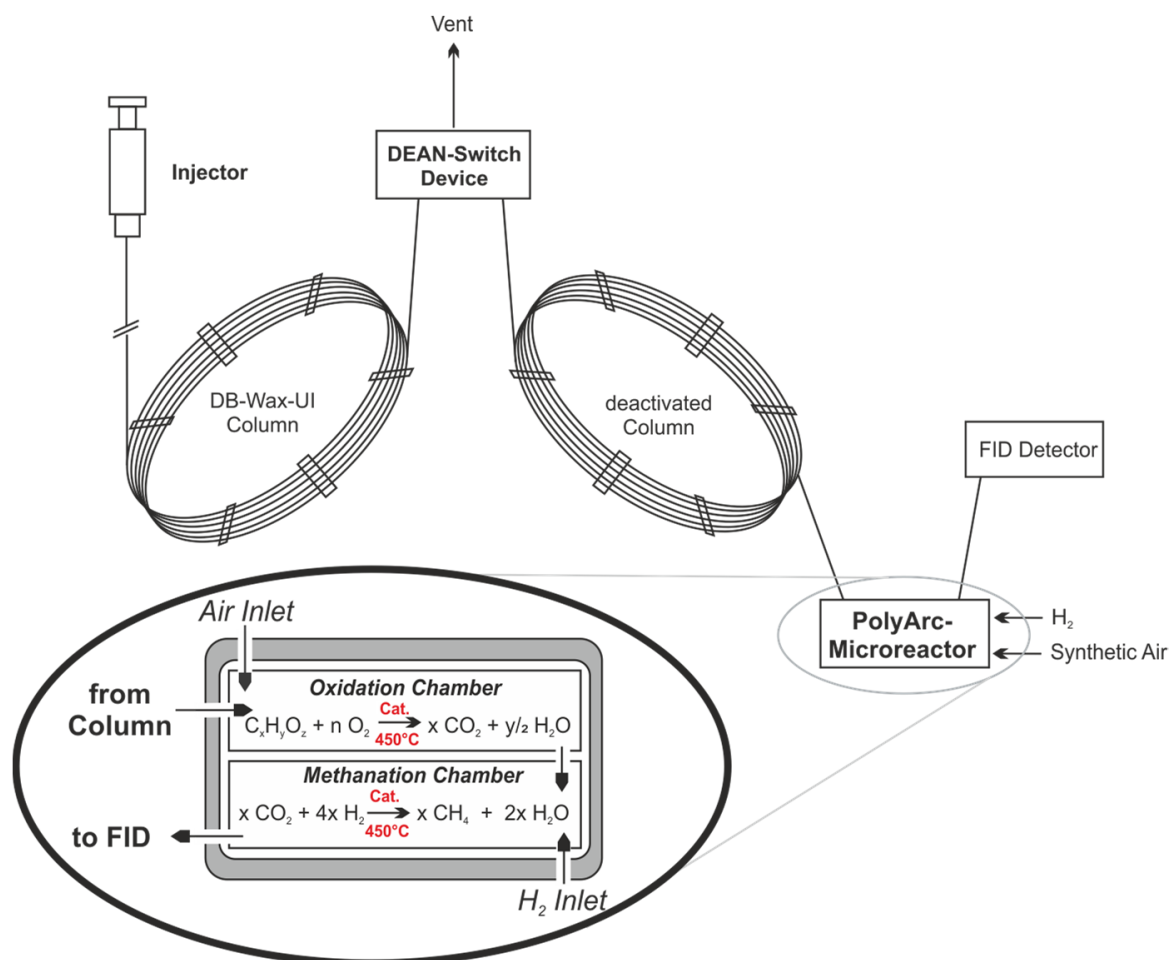


Figure 14. Working principle of the optimised GC analytics with protecting Dean switch and the catalytic two-chamber micro reactor for methanisation of analytes (PolyArc) [49,50].

4. Conclusions

An extensive study on ruthenium and ruthenium-nickel catalysts supported on γ -Al₂O₃ was performed, showing interesting connections between synthetic pathways, re-

sulting material structures and the observed catalytic activity during CO hydrogenation conducted in methanol. The results clearly showed the connection between the synthesis parameters, including variation of loading, precursor or the co-impregnation of nickel. These interlinks could be seen in the characterisation techniques, such as the temperature-programmed reactions, X-ray diffraction measurements or scanning electron microscopy. Furthermore, the result of this difference in catalyst structure also impacted the catalytic activity. All of the synthesised catalysts were active in the carbonylation of methanol to methylformate. The ruthenium on alumina catalysts showed a higher productivity for methyl formate at higher loadings. The variation of the precursor did not have a great impact on the productivity towards methyl formate: only a slightly increased productivity towards methyl formate of the Ru-Cl-XX-icr. catalysts compared to the Ru-NO-XX-icr. catalysts was observed at 90 °C. At higher temperatures, the Ru-NO-5-icr. catalyst had a higher productivity than the Ru-Cl-5-icr., with the shift happening between 110 and 130 °C. Generally one can say that higher temperatures and higher partial pressure for carbon monoxide enhanced the methyl formate productivity. This led to the highest reaction rate reached during this study of $0.142 \pm 0.004 \text{ mol} \cdot \text{L}^{-1} \cdot \text{g}^{-1} \cdot \text{h}^{-1}$ (90% CO, 10% H₂, 150 °C). Generally, the co-impregnation of nickel led to an inhibition of the carbonylation reaction of methanol. The methanol-mediated CO hydrogenation on catalysts with high chloride loadings showed an activity towards the formation of dimethoxymethane. One can conclude from this fact that bifunctional catalysts with both acidic and hydrogenation component are needed to directly reduce carbon monoxide to the formaldehyde oxidation state. The presence of a protic solvent further stabilises formaldehyde in its hemiacetal form; however, this stabilisation is not high enough to prevent a further acid-catalysed reaction and leads eventually to the full acetal. This reaction, however, allows us to gain indirectly valuable information on the formation of formaldehyde generated via CO hydrogenation.

Supplementary Materials: The following supporting information can be downloaded at: <https://www.mdpi.com/article/10.3390/catal13030482/s1>, Figure S1: Comparison of particle size and MeFo productivity for the Ru-XX catalysts. Figure S2: SEM-EDX pictures of Ru-NO-1-icr. catalyst. Figure S3: SEM-EDX pictures of Ru-NO-3-icr. catalyst. Figure S4: SEM-EDX pictures of Ru-NO-5-icr. catalyst. Figure S5: SEM-EDX pictures of Ru-Cl-1-icr. catalyst. Figure S6: SEM-EDX pictures of Ru-Cl-3-icr. catalyst. Figure S7: SEM-EDX pictures of Ru-Cl-5-icr. catalyst. Figure S8: SEM-EDX pictures of RuNi-NO-ir. catalyst. Figure S9: SEM-EDX pictures of RuNi-NO-icr. catalyst. Figure S10: SEM-EDX pictures of RuNi-Cl-ir. catalyst. Figure S11: SEM-EDX pictures of RuNi-Cl-icr. catalyst. Figure S12: Pictures of the PASCAR plant used for all catalyst screening experiments and for parameter studies. Figure S13: Picture of the gas chromatograph used for the off-line analysis of samples. Figure S14: Exemplary chromatogram of a measurement of the CO-Hydrogenation in methanolic media after 24 h with the use of a Ru-NO-3 catalyst; Table S1: Comparison of H₂ uptake and metal loading.

Author Contributions: K.A.S.: conceptualisation, methodology, software, validation, formal analysis, investigation, data curation, writing—original draft preparation, writing—reviewing and editing, visualisation. R.D.: conceptualisation, methodology, resources. T.A.Z.: conceptualisation, software, validation, formal analysis, visualisation, supervision, writing—original draft preparation, writing—reviewing and editing. J.S.: funding acquisition, conceptualisation, supervision, investigation, writing, reviewing and editing. M.B.: funding acquisition, conceptualisation, supervision, investigation, writing, reviewing and editing. All authors have read and agreed to the published version of the manuscript.

Funding: The authors gratefully acknowledge financial support from the Bundesministerium für Bildung und Forschung (BMBF) within the NAMOSYN Project (FKZ 03SF0566K0).

Data Availability Statement: The data presented in this study are available on request from the corresponding author. The data are not publicly available due to confidential reasons.

Acknowledgments: We thank Armin Lautenbach and Michael Zimmermann for analytical assistance. We acknowledge support by the KIT-Publication Fund of the Karlsruhe Institute of Technology.

Conflicts of Interest: The authors declare no conflict of interest.

References

1. Jacob, E. C-1 Oxygenate als nachhaltige Kraftstoffe und deren günstige Eigenschaften. In *Zukünftige Kraftstoffe: Energiewende des Transports als ein Weltweites Klimaziel*; Maus, W., Ed.; Springer: Berlin/Heidelberg, Germany, 2019; pp. 155–180.
2. Oestreich, D. *Prozessentwicklung zur Gewinnung von Oxymethylenethern (OME) aus Methanol und Formaldehyd*; KIT Scientific Publishing: Karlsruhe, Germany, 2017.
3. Bahmanpour, A.M.; Hoadley, A.; Tanksale, A. Formaldehyde production via hydrogenation of carbon monoxide in the aqueous phase. *Green Chem.* **2015**, *17*, 3500–3507. [[CrossRef](#)]
4. Bahmanpour Ali, M. *Single-Step Conversion of Synthesis Gas into Formaldehyde*; Monash University: Melbourne, Australia, 2016.
5. Ahmad, W.; Chan, F.L.; Hoadley, A.; Wang, H.; Tanksale, A. Synthesis of oxymethylene dimethyl ethers (OMEn) via methanol mediated COx hydrogenation over Ru/BEA catalysts. *Appl. Catal. B Environ.* **2020**, *269*, 118765. [[CrossRef](#)]
6. Ahmad, W.; Chan, F.L.; Chaffee, A.L.; Wang, H.; Hoadley, A.; Tanksale, A. Dimethoxymethane Production via Catalytic Hydrogenation of Carbon Monoxide in Methanol Media. *ACS Sustain. Chem. Eng.* **2020**, *8*, 2081–2092. [[CrossRef](#)]
7. Remediakis, I.N.; Abild-Pedersen, F.; Nørskov, J.K. DFT Study of Formaldehyde and Methanol Synthesis from CO and H₂ on Ni(111). *J. Phys. Chem. B* **2004**, *108*, 14535–14540. [[CrossRef](#)]
8. Munnik, P.; de Jongh, P.E.; de Jong, K.P. Recent Developments in the Synthesis of Supported Catalysts. *Chem. Rev.* **2015**, *115*, 6687–6718. [[CrossRef](#)]
9. Swain, P.; Mallika, C.; Srinivasan, R.; Mudali, U.K.; Natarajan, R. Separation and recovery of ruthenium: A review. *J. Radioanal. Nucl. Chem.* **2013**, *298*, 781–796. [[CrossRef](#)]
10. Mazzieri, V.; Coloma-Pascual, F.; González, M.; L'argentičre, P.; Figoli, N. Preparation of Ru/Al₂O₃ Catalysts from RuCl₃. *React. Kinet. Catal. Lett.* **2002**, *76*, 53–59. [[CrossRef](#)]
11. Düllmann, C.E.; Eichler, B.; Eichler, R.; Gäggeler, H.W.; Türler, A. On the Stability and Volatility of Group 8 Tetroxides, MO₄ (M = Ruthenium, Osmium, and Hassium (Z = 108)). *J. Phys. Chem. B* **2002**, *106*, 6679–6684. [[CrossRef](#)]
12. Betancourt, P.; Rives, A.; Hubaut, R.; Scott, C.E.; Goldwasser, J. A study of the ruthenium–alumina system. *Appl. Catal. A Gen.* **1998**, *170*, 307–314. [[CrossRef](#)]
13. Balcerzak, M.; Świącicka, E.; Balukiewicz, E. Determination of platinum and ruthenium in Pt and Pt–Ru catalysts with carbon support by direct and derivative spectrophotometry. *Talanta* **1999**, *48*, 39–47. [[CrossRef](#)]
14. Balcerzak, M. Analytical Methods for the Determination of Ruthenium: The State of the Art. *Crit. Rev. Anal. Chem.* **2002**, *32*, 181–226. [[CrossRef](#)]
15. Chang, X.-J.; Gong, B.-L.; Su, Z.-X.; Yang, D.; Luo, X.-Y. ICP-OES determination of traces of Ru, Au, V and Ti preconcentrated and separated by a new poly(epoxy-melamine) chelating resin from solutions. *Fresenius J. Anal. Chem.* **1998**, *360*, 736–739. [[CrossRef](#)]
16. Suoranta, T.; Niemelä, M.; Perämäki, P. Comparison of digestion methods for the determination of ruthenium in catalyst materials. *Talanta* **2014**, *119*, 425–429. [[CrossRef](#)] [[PubMed](#)]
17. Zou, Z.; Wang, Z.; Cheng, H.; He, T.; Liu, Y.; Chen, K.; Hu, Z.; Liu, Y. Comparative Determination of Mass Fractions of Elements with Variable Chalcophile Affinities in Geological Reference Materials with and without HF-desilicification. *Geostand. Geoanal. Res.* **2020**, *44*, 501–521. [[CrossRef](#)]
18. Grillo, F.; Van Bui, H.; Moulijn, J.A.; Kreutzer, M.T.; van Ommen, J.R. Understanding and Controlling the Aggregative Growth of Platinum Nanoparticles in Atomic Layer Deposition: An Avenue to Size Selection. *J. Phys. Chem. Lett.* **2017**, *8*, 975–983. [[CrossRef](#)]
19. Grillo, F.; Soethoudt, J.; Marques, E.A.; de Martín, L.; Van Dongen, K.; van Ommen, J.R.; Delabie, A. Area-Selective Deposition of Ruthenium by Area-Dependent Surface Diffusion. *Chem. Mater.* **2020**, *32*, 9560–9572. [[CrossRef](#)]
20. Lin, B.; Wang, R.; Lin, J.; Du, S.; Yu, X.; Wei, K. Preparation of chlorine-free alumina-supported ruthenium catalyst for ammonia synthesis base on RuCl₃ by hydrazine reduction. *Catal. Commun.* **2007**, *8*, 1838–1842. [[CrossRef](#)]
21. Rynkowski, J.M.; Paryjczak, T.; Lenik, M. Characterization of alumina supported nickel-ruthenium systems. *Appl. Catal. A Gen.* **1995**, *126*, 257–271. [[CrossRef](#)]
22. Rynkowski, J.; Paryjczak, T.; Lenik, M. On the nature of oxidic nickel phases in NiO/γ-Al₂O₃ catalysts. *Appl. Catal. A Gen.* **1993**, *106*, 73–82. [[CrossRef](#)]
23. Ping, D.; Wan, Y.; Zhao, X.; Geng, J.; Dong, X. Zr-promoted nickel-rich spinel-supported Ni catalysts with enhanced performance for selective CO methanation. *Int. J. Energy Res.* **2022**, *46*, 9128–9137. [[CrossRef](#)]
24. Khalighi, R.; Bahadoran, F.; Panjeshahi, M.H.; Zamaniyan, A.; Tahouni, N. Effects of Nickel Aluminate Spinel (NiAl₂O₄) as Catalyst Support and Promoters (Ru, Rh) in Fischer-Tropsch Synthesis. *ChemistrySelect* **2020**, *5*, 7934–7940. [[CrossRef](#)]
25. Hull, A.W. X-ray crystal analysis of thirteen common metals. *Phys. Rev.* **1921**, *17*, 571. [[CrossRef](#)]
26. Wynblatt, P.; Gjostein, N.A. Supported metal crystallites. *Prog. Solid State Chem.* **1975**, *9*, 21–58. [[CrossRef](#)]
27. Miranda, M.; Sasaki, J. The limit of application of the Scherrer equation. *Acta Crystallogr. Sect. A Found. Adv.* **2018**, *74*, 54–65. [[CrossRef](#)]
28. Muniz, F.T.L.; Miranda, M.R.; dos Santos, C.M.; Sasaki, J.M. The Scherrer equation and the dynamical theory of X-ray diffraction. *Acta Crystallogr. Sect. A Found. Adv.* **2016**, *72*, 385–390. [[CrossRef](#)]
29. Nandanwar, S.U.; Chakraborty, M.; Mukhopadhyay, S.; Shenoy, K.T. Stability of ruthenium nanoparticles synthesized by solvothermal method. *Cryst. Res. Technol.* **2011**, *46*, 393–399. [[CrossRef](#)]
30. Chen, L.; Zhu, Y.; Zheng, H.; Zhang, C.; Zhang, B.; Li, Y. Aqueous-phase hydrodeoxygenation of carboxylic acids to alcohols or alkanes over supported Ru catalysts. *J. Mol. Catal. A Chem.* **2011**, *351*, 217–227. [[CrossRef](#)]

31. Hosokawa, S.; Kanai, H.; Utani, K.; Taniguchi, Y.-I.; Saito, Y.; Imamura, S. State of Ru on CeO₂ and its catalytic activity in the wet oxidation of acetic acid. *Appl. Catal. B Environ.* **2003**, *45*, 181–187. [[CrossRef](#)]
32. Sun, F.; Chen, L.; Weng, Y.; Wang, T.; Qiu, S.; Li, Q.; Wang, C.; Zhang, Q.; Ma, L. Transformation of biomass polyol into hydrocarbon fuels in aqueous medium over Ru-Mo/CNT catalyst. *Catal. Commun.* **2017**, *99*, 30–33. [[CrossRef](#)]
33. Cattania, M.G.; Parmigiani, F.; Ragaini, V. A study of ruthenium catalysts on oxide supports. *Surf. Sci.* **1989**, *211–212*, 1097–1105. [[CrossRef](#)]
34. Guzzi, L.; Schay, Z.; Matusek, K.; Bogyay, I. Surface structure and selectivity control in the CO + H₂ reaction over FeRu Bimetallic catalysts. *Appl. Catal.* **1986**, *22*, 289–309. [[CrossRef](#)]
35. Pinheiro, A.N.; Valentini, A.; Sasaki, J.M.; Oliveira, A.C. Highly stable dealuminated zeolite support for the production of hydrogen by dry reforming of methane. *Appl. Catal. A Gen.* **2009**, *355*, 156–168. [[CrossRef](#)]
36. Crisafulli, C.; Scirè, S.; Minicò, S.; Solarino, L. Ni–Ru bimetallic catalysts for the CO₂ reforming of methane. *Appl. Catal. A Gen.* **2002**, *225*, 1–9. [[CrossRef](#)]
37. Arif, N.N.M.; Abidin, S.Z.; Osazuwa, O.U.; Vo, D.-V.N.; Azizan, M.T.; Taufiq-Yap, Y.H. Hydrogen production via CO₂ dry reforming of glycerol over ReNi/CaO catalysts. *Int. J. Hydrogen Energy* **2019**, *44*, 20857–20871. [[CrossRef](#)]
38. Moreno, A.Á.; Ramirez-Reina, T.; Ivanova, S.; Roger, A.-C.; Centeno, M.Á.; Odriozola, J.A. Bimetallic Ni–Ru and Ni–Re catalysts for dry reforming of methane: Understanding the synergies of the selected promoters. *Front. Chem.* **2021**, *9*, 694976. [[CrossRef](#)] [[PubMed](#)]
39. Andraos, S.; Abbas-Ghaleb, R.; Chlala, D.; Vita, A.; Italiano, C.; Laganà, M.; Pino, L.; Nakhil, M.; Specchia, S. Production of hydrogen by methane dry reforming over ruthenium-nickel based catalysts deposited on Al₂O₃, MgAl₂O₄, and YSZ. *Int. J. Hydrogen Energy* **2019**, *44*, 25706–25716. [[CrossRef](#)]
40. Low, G.G.; Bell, A.T. Studies of CO desorption and reaction with H₂ on alumina-supported Ru. *J. Catal.* **1979**, *57*, 397–405. [[CrossRef](#)]
41. Low, G.G. *Temperature-Programmed Desorption and Reaction of CO and H₂ on Alumina-Supported Ruthenium Catalyst*; U.S. Department of Energy Office of Scientific and Technical Information: Oak Ridge, TN, USA, 1978.
42. Kang, J.; Zhang, S.; Zhang, Q.; Wang, Y. Ruthenium Nanoparticles Supported on Carbon Nanotubes as Efficient Catalysts for Selective Conversion of Synthesis Gas to Diesel Fuel. *Angew. Chem. Int. Ed.* **2009**, *48*, 2565–2568. [[CrossRef](#)]
43. Yang, E.; Jang, E.J.; Lee, J.G.; Yoon, S.; Lee, J.; Musselwhite, N.; Somorjai, G.A.; Kwak, J.H.; An, K. Acidic effect of porous alumina as supports for Pt nanoparticle catalysts in n-hexane reforming. *Catal. Sci. Technol.* **2018**, *8*, 3295–3303. [[CrossRef](#)]
44. Kaiser, D.; Beckmann, L.; Walter, J.; Bertau, M. Conversion of Green Methanol to Methyl Formate. *Catalysts* **2021**, *11*, 869. [[CrossRef](#)]
45. Černohorský, M. The ratio method for absolute measurements of lattice parameters with cylindrical cameras. *Acta Crystallogr.* **1960**, *13*, 823–826. [[CrossRef](#)]
46. Lejus, A. Formation at high temperature of nonstoichiometric spinels and of derived phases in several oxide systems based on alumina and in the system alumina–aluminum nitride. *Rev. Int. Hautes Temp. Refract* **1964**, *1*, 53–95.
47. Hull, A.W. A new method of X-ray crystal analysis. *Phys. Rev.* **1917**, *10*, 661. [[CrossRef](#)]
48. Papoulis, A. *Proceedings*; Polytechnic Institute of Brooklyn Brooklyn, Interscience Publishers: New York, NY, USA, 1967; p. 87.
49. Spanjers, C.S.; Beach, C.A.; Jones, A.J.; Dauenhauer, P.J. Increasing flame ionization detector (FID) sensitivity using post-column oxidation–methanation. *Anal. Methods* **2017**, *9*, 1928–1934. [[CrossRef](#)]
50. Jorgensen, A.D.; Picel, K.C.; Stamoudis, V.C. Prediction of gas chromatography flame ionization detector response factors from molecular structures. *Anal. Chem.* **1990**, *62*, 683–689. [[CrossRef](#)]

Disclaimer/Publisher’s Note: The statements, opinions and data contained in all publications are solely those of the individual author(s) and contributor(s) and not of MDPI and/or the editor(s). MDPI and/or the editor(s) disclaim responsibility for any injury to people or property resulting from any ideas, methods, instructions or products referred to in the content.